Passive Imaging Based Hazard Avoidance for Spacecraft Safe Landing

Yang Cheng, Andrew E. Johnson, Larry H. Mattheis, Aron A. Wolf
Jet Propulsion Laboratory, California Institute of Technology
4800 Oak Grove Drive, Pasadena, CA 91109-8099
Tele: (818) 354-1857, FAX (818) 393-4085, Email: ycheng@telerobotics.jpl.nasa.gov

Keywords: Spacecraft safe landing, passive imaging, homography transform, slope estimation, hazard avoidance, planetary exploration.

Abstract

During planetary landing, safety is critical for mission success. Hazard avoidance is an approach to safe landing that guides the spacecraft to a benign landing site through onboard analysis of sensed data. In this paper, a new and fast passive sensing based hazard avoidance approach for spacecraft safe landing is suggested. This approach contains two important algorithms: a texture based landing site selection algorithm and a landing site slope estimation algorithm. Using this new approach, a safe landing site can be selected in real time while the spacecraft is descending. Since the surface slope is a very important factor for safe landing and rover mobility, an error analysis of the slope estimation algorithm is given. Finally, experimental results on real descent imagery are shown.

1. Introduction

In the outline of NASA's Mars Exploration Program for next two decades, NASA proposes to develop and launch a long-range, long duration mobile science laboratory. This mobile platform will provide a major increase in surface measurements and will pave the way for a future sample return mission. NASA is studying options to launch this mobile science laboratory mission as early as 2007. This mission will also demonstrate the technology for accurate landing and hazard avoidance in order to reach what may be very promising but difficult-to-reach scientific sites.

Two types of sensors, active and passive sensors, can be used for hazard avoidance. The active sensors, such as radar, lidar, supply their own source of energy to illuminate feature of interest and the passive sensor, such as camera, sense naturally available energy. Because the active sensors such as lidar can directly measure range to the sensed terrain and their data processing algorithms are relatively simple and fast, the active sensing hazard avoidance is considered the most promising method for future missions [5]. However, active sensors have their own generic disadvantages. For example, they are often more expensive, heavier and have higher power consumption. In contrast to active sensors, passive sensors (camera) possess lower mass, lower cost, lower power consumption and higher resolution. Most importantly, the current state-of-the-art technology of passive imaging in space is much more mature than other types of sensing and therefore less risk will be introduced by sensor design. The biggest disadvantage of the passive sensing method is that the conventional algorithms involved are computationally too slow for safe landing on planetary bodies. In this paper, we suggest a novel hazard avoidance approach using passive imagery. In this approach, the computational efficiency of the passive sensing has been greatly improved through appropriate use of the spacecraft trajectory, careful timing of sensing and selective processing of the data. Our initial study shows that the proposed method can perform hazard detection at the speeds and reliability required for planetary safe landing.

1.1 The Safe Landing Criteria

Preliminary engineering constraints for safe landing are derived from the spacecraft design and landing scenario as defined for the future mission. According to the current Mars 2007 Smart Lander baseline, a safe landing site should satisfy these constrains:

- The surface slope must be below 15 degrees;
- The probability of landing on a rock > 33 cm high should be less than about 1%.

Because a detailed local surface map does not exist and the spacecraft has a large landing error ellipse, hazard detection and avoidance must be done in real time while the spacecraft is descending. Hazard avoidance will start when the spacecraft enters the final stage of powered descent, which occurs approximately 1000 meters above the ground. At this moment, the vertical descent velocity is about 40 m/s +/-15% and horizontal velocity is less than +/-20 m/s [3]. Powered descent lasts

approximately 30 seconds. In order to select a suitable landing site and give the spacecraft time to maneuver, the system is required to perform hazard detection in one second, which is extremely challenging.

1.2 Current State of the Art of the Passive Sensing

If a conventional passive imaging method [1], which is also called structure from motion (SfM), is employed, hazard detection is accomplished in multiple steps:

- **Feature Matching** detects and matches the features from two image frames;
- **Motion Adjustment** refines the motion parameters provided by onboard inertial sensors to comply with the epipolar constraints by using the matched features;
- **Depth Recovery** correlates adjacent frames to match pixels for surface reconstruction;
- **Hazard Detection** detects any hazards presented in the depth map and selects a suitable landing site.

The conventional algorithms involved in each step are often computationally expensive and they are excessively slow for the planetary safe landing application. For instance, the algorithm in [1] takes 10 seconds for the feature matching step, 14 seconds for the motion adjustment step and 81 seconds for depth recovery step for two 896 by 896 images on a SUN Ultra 10 workstation. Obviously this speed is not acceptable. However some strategies exist to reduce and even eliminate some of those computations.

- The objective of motion refinement is to establish the precise camera motion between any two frames so that epipolar constraints are satisfied to sub-pixel accuracy and the depth can be recovered by just searching along the epipolar lines. However, when the pixel correlation match is not involved, such a highly accurate motion might not be needed. In other words, the motion provided by the onboard inertial sensors might be adequate.
- Because spacecraft's maneuvering capability is very limited (<50m), the landing site is confined in a small portion of an image scene. Therefore, we only need to examine a small subset of an image when the image coverage is larger than the spacecraft maneuvering capability.
- Potentially "unsafe" regions can be computed quickly from a single image by finding areas that are highly textured, in shadow, or near the image edges. Because the spacecraft should not land in these "unsafe" areas, future examination of these areas becomes unnecessary.

2 A New Passive Imaging Based Hazard Avoidance Algorithm

2.1 Safe Landing Sites Selection

According to the safe landing criteria, the landing site should be free from large rocks (smoothness), flat and level. The smoothness (homogeneity) of a landing surface can be indirectly measured by image intensity variation, such as the image intensity standard deviation (ISD).

$$ISD(i,j) = \frac{1}{(2w+1)^2} \{ \sum_{p=i-w}^{p=i+w} \sum_{q=j-w}^{q=j+w} I(p,q)^2 - \frac{1}{(2w+1)} [\sum_{p=i-w}^{p=i+w} \sum_{q=j-w}^{q=j-w} I(p,q)]^2 \}$$

(1)

where I is the image intensity value, w is the half window size, which is dependent on the current height of spacecraft, the camera's field of view (FOV), and the lander size.

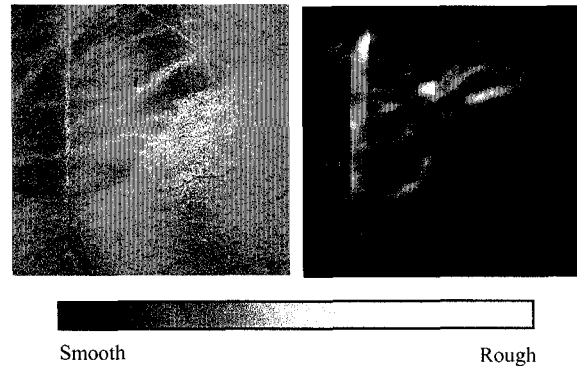Smooth   Rough

Figure 1: The image intensity standard deviation corresponds heuristically to the surface smoothness

The lower the ISD is, the smoother the area is (see Fig. 1). Some regions, which may in fact be safe with respect to surface roughness, will have a high ISD. Therefore by eliminating regions with a high ISD all rough regions in the image will be eliminated quickly at the expense of eliminating some regions, which are in fact safe.

In order to find the best landing site, the possible landing area is divided into multiple regions separated by half window size buffer zones. In each region, a candidate site with minimal ISD is selected. Because these regions are separated by the buffer zone, the landing site candidates would not fully overlap each other (see Fig. 2).

We take a dynamic updating technique, which is commonly used by stereo matching, to speed up the computation. In this technique, the current ISD is computed by subtracting the first column of the last ISD and adding the last column in the current window (see Fig. 3). The same strategy is used on row wise rolling. This technique takes only 900 ms on a 1000 by 1000 image on a Sun Ultra 10 workstation. Additional speedup is also achieved by resampling the image at a coarser resolution. It takes only 220 ms on a 500 by 500 image and 90 ms on a 250 by 250 image. It is worthwhile to point out that fairly consistent results are obtained from different resolution images (see Fig. 4). Therefore using lower resolution image for the initial landing site selection can save substantial time, which can be used for other computations, such as data preprocessing, navigation etc.
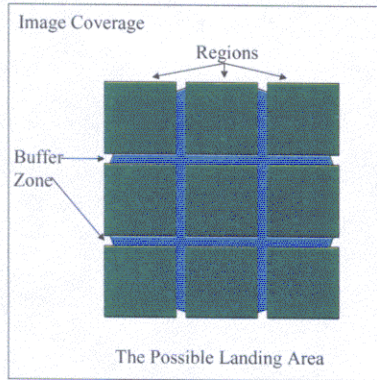

Figure 2: The possible landing area is divided into multiple regions separated by half window size buffer zone. A landing site candidate with lowest ISD is selected in each region.
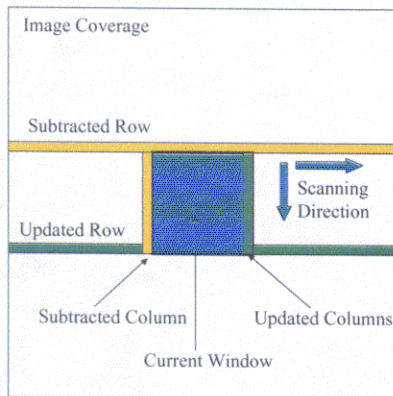

Figure 3: The dynamic updating technique can greatly increase the speed of landing site selection processing.
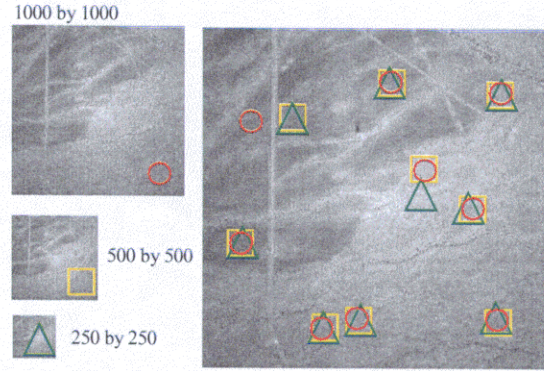

Figure 4: The locations of landing site candidates selected from different resolutions of image are fairly consistent. The image on right side shows all landing site selected from different resolutions images. Circles, squares, and triangles represent the landing sites selected from images of original, 2x and 4x coarser resolutions respectively.

2.2 Slope Computation

Although these selected candidates represent the smoothest area in each region, other type of hazard, such as steep slope, might exist in these sites. In order to pick up the best landing site, the slope of these candidate have to be determined. At here the slope is computed based on the perspective relationship of the sites between two adjacent descent images.

2.2.1 Homography and Its Geometric Meaning

Homography defines the relationship of a plane between two images by an eight-parameter perspective transform [2][4] (see Fig. 5)

$$x' = \begin{bmatrix} u' \\ v' \\ 1 \end{bmatrix} \cong Px = \begin{bmatrix} p_0 & p_1 & p_2 \\ p_3 & p_4 & p_5 \\ p_6 & p_7 & 1 \end{bmatrix} \begin{bmatrix} u \\ v \\ 1 \end{bmatrix} \qquad (2)$$

where $x = (u, v, 1)^T$ and $x' = (u', v', 1)^T$ are homogeneous coordinates, and $\cong$ indicates equality up to scale.

The homography transform has been used successfully in video mosaics [2], 3D scene analysis [4], feature matching [7] etc. It is also suitable for the safe landing purpose because we are most interested in landing a spacecraft at a flat area (a plane). The perspective relationship between the two images not only represents the motion between the two images but also indicates the slope of the represented area. Another advantage of

the homography transform is that it does not need image pixel correspondence for the homography construction. Therefore the feature detection, matching, and even some of the motion refinement can be avoided.
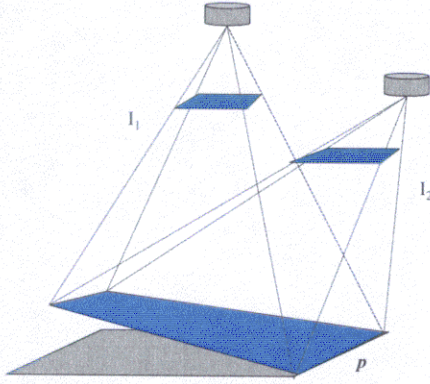

Figure 5: A homography transform defines the relationship of a plane in two images.

Let's rewrite the transform as

$$u' = \frac{p_0 u + p_1 v + p_2}{p_6 u + p_7 v + 1}$$
$$v' = \frac{p_3 u + p_4 v + p_5}{p_6 u + p_7 v + 1}$$

(3)

The eight parameters in equation (3) can be determined iteratively by minimizing a merit function

$$M_0 = \sum [\alpha I_0(Qx') + \beta - I_1(x')]^2 = \sum e^2$$

or

(4)

$$M_1 = \sum [I_0(x) - \frac{1}{\alpha} I_1(Px) - \frac{\beta}{\alpha}]^2 = \sum e^2$$

where α, β in equation (4) are the parameters of a linear image intensity correction [4] and Q is the inverse transform of P. The M_0 and M_1 are equivalent, but M_0 is faster to compute. We will explain the reason later.

The minimization algorithm, the Levenberg-Marquardt iterative algorithm [2][4], requires computation of the partial derivatives of M_0 with respect to the unknown parameters $\{q_0 \dots q_7\}$.

$$\frac{\partial M_0}{\partial q_0} = \frac{u'}{D}\frac{\partial I_0}{\partial u}, \dots, \frac{\partial M_0}{\partial q_7} = -\frac{v'}{D}(u\frac{\partial I_0}{\partial u} + v\frac{\partial I_0}{\partial v})$$

where D is the denominator in equation (3) and ($\partial I_0/\partial u$, $\partial I_0/\partial v$) is the image intensity gradient of I_0 at (u, v).

In [2] and [4], the image intensity gradient is recomputed in each iteration, which is too costly. In

order to reduce the computation, we fix the windows and image intensity gradient in the first image and they are inversely projected to the second image based on the newly obtained transform. In this way, the image gradient only needs to be computed once at the beginning.

Because of a possible large variation in scale and/or rotation due to fast and uneven descent, the straightforward methods for homography construction in [2][4] do not always work. In order to ensure the transform can be obtained, an initial homography transform, which is approximated to the true transform, is needed. This initial transform can be obtained by using the spacecraft altitude, attitude, and motion between the images. Then the progressive method suggested in [4] is used. In this method the homography is computed hierarchically: only translation (q_2 and q_5) is involved in the minimization at the coarsest level, then the scale and rotation $\{q_0 \dots q_5\}$ are refined at the middle level and the perspective transform $\{q_0 - q_7\}$ is computed at the finest level. The output of the optimization is the homography transform, the residual of equation (4) and the correlation between the two windows.

When a site is perfectly flat, the relationship of the site between two descent images satisfies equation (2) exactly. However, when the site is not perfectly flat, equation (2) defines a plane that passes through the site. In this case the residual of equation (4) indicates the roughness of the site (see Fig. 6).
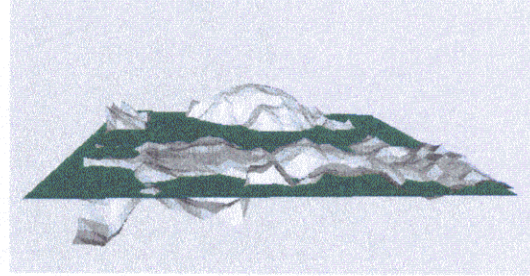

Figure 6: When the terrain is not perfectly flat, the homography transform defines a plane passing through the surface.

2.2.2 Slope Computation

There are two possible ways to compute the slopes of the landing sites. First, when the motion provided by onboard sensors is within the accuracy requirements, the slope can be obtained by direct triangulation. For example, the pixels corresponding to the four corners of a landing site in the first image can be found in the second image by using the homography transform obtained from previous section. Given the correspondences and the homography, the 3D positions

of the corners and the associated slope of the landing site can be readily determined.

When the onboard sensors cannot provide sufficiently accurate motion information, there is still a way to compute the slope. As matter of fact, the eight parameters of a homography transform contain enough information to recover both the spacecraft motion between images and the slope of the landing site. If R represents the rotation between the two coordinate systems and T represents the 3D translation between the two views, the relation of R, T and P is

$$P \cong V(R + T(a,b,c))V^{-1} \qquad (5)$$

where (a, b, c) represents a plane determined by the homography transform:

$$aX + bY + cZ = 1 \qquad (6)$$

and

$$V = \begin{bmatrix} f_h & 0 & 0 \\ 0 & f_v & 0 \\ 0 & 0 & 1 \end{bmatrix} \qquad (7)$$

where f_h and f_v are horizontal and vertical focal length.

Again with initial R and T, (a, b, c) can be determined by an optimization process [4].

2.2.3 Error Analysis

Two types of errors (position and attitude) can be introduced if the onboard inertial sensor data is directly used in the slope estimation. We would like to know how those errors effect the slope estimation.

2.2.3.1 The Slope Error Caused by Position Error

Suppose two images are taken at position A and B, CZ is a flat and level ground and C is a point on CZ. When a position error (db) is involved, the new position of C recovered from the disparity of the two images will be at C' (see Fig 7).

When the spacecraft height is Z,
$AC = Z/\cos r$
$AC' = AB' \, AC/AB = bZ/[(b+db)\cos r]$
and
$Z' = AC'^*\cos r = bZ/(b+db)$

Obviously, Z' is independent from r. Therefore the position error would not cause any error in slope estimation.
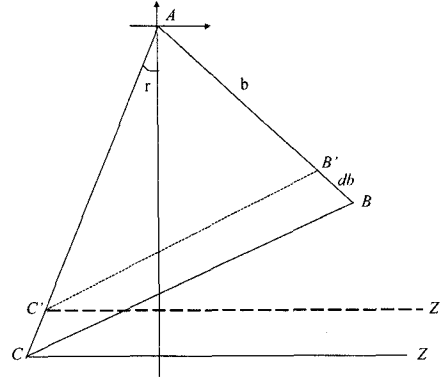

Figure 7: The position error will not cause slope error.

2.2.3.2 The Slope Error Caused by Attitude Error

Again, we assume the spacecraft is descending at an angle β and two images are taken at A and B and the distance between A and B is b (see Fig. 8). An attitude error ($\Delta\varphi$) will move a point C on a leveled plane CZ to a new position C'.

From Fig. 8, we can easily get

$$x_c = z \tan \gamma \qquad z_c = z$$
$$x_b = b \cos \beta \qquad y_b = b \sin \beta \qquad (8)$$
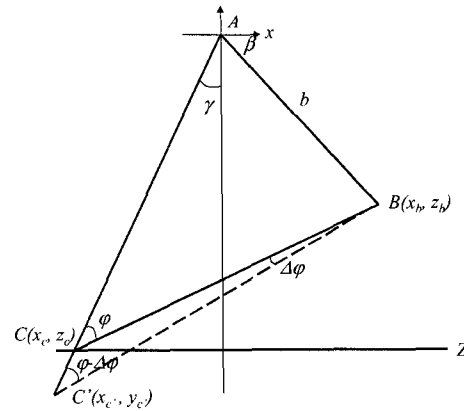
where γ is the angle between an optical ray and nadir vector.

Figure 8: The slope error is a function of an attitude error, distance between two images and descending angle.

Therefore, we have

$$x_{c'} = x_c + CC' \sin \gamma$$
$$z_{c'} = z_c + CC' \cos \gamma \qquad (11)$$

The slope error (dS), therefore, is:

$$dS = \frac{dz_{c'}}{d\gamma} / \frac{dx_{c'}}{d\gamma} \qquad (12)$$

Where

$$CC' = \frac{BC \sin \Delta\varphi}{\sin(\varphi - \Delta\varphi)} = \frac{b \cos(\gamma - \beta) \sin \Delta\varphi}{\sin\varphi \sin(\varphi - \Delta\varphi)}$$

$$BC = \frac{b \cos(\gamma - \beta)}{\sin\varphi}$$

$$\frac{dx_{c'}}{d\gamma} = \frac{z}{\cos^2\gamma} + \frac{dCC'}{d\gamma}\sin\gamma + CC\cos\gamma$$

$$\frac{dz_{c'}}{d\gamma} = \frac{dCC'}{d\gamma}\cos\gamma - CC'\sin\gamma$$

$$\frac{dCC'}{d\gamma} = -\frac{b \cos(\gamma - \beta) \sin \Delta\varphi}{\sin\varphi \sin(\varphi - \Delta\varphi)}$$
$$-\frac{b \cos(\gamma - \beta) \sin \Delta\varphi}{\sin^2\varphi \sin^2(\varphi - \Delta\varphi)}\sin(2\varphi - 2\Delta\varphi)\frac{d\varphi}{d\gamma}$$

$$\varphi = 90 - \gamma - \arctan\frac{z - b\sin\beta}{z\tan\gamma - b\cos\beta}$$

$$\frac{d\varphi}{d\gamma} = (z - b\sin\beta)z / \{(z\tan\gamma - b\cos\beta)^2 +$$
$$(z - b\sin\beta)^2]\cos^2\gamma\} - 1$$

From this analysis, we find that slope estimation error is a function of three primary factors: the baseline length to spacecraft height ratio (BHR), the descent angle β and attitude error (AE). In general, the higher BHR or lower AE, the lower the slope estimation error is (see Fig. 9 & 10).
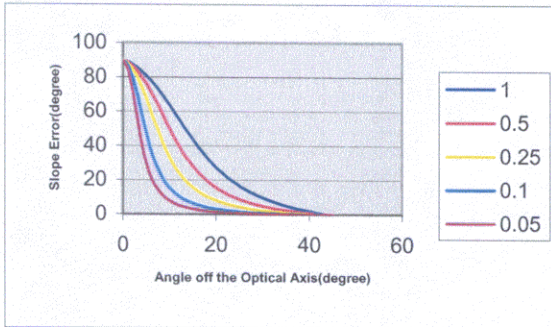

Figure 9: The relationship between the attitude error and the error of slope estimation is shown. In this case, the baseline to height ratio (BHR) is 1:20 and the spacecraft is descending vertically.

The descent angle is the most interesting factor. For example, if the spacecraft is descending vertically, the largest error of slope estimation (blind data spot (BDS)) will be at the center of the image. In this case, the slope estimation is so sensitive to the attitude error that motion refinement becomes necessary. If the spacecraft descends at a 45-degree angle, the BDS will move out of the image scene. In this case, even when the AR is large (0.1 degree) and the BHR is small (1/20), the slope estimation error is less than 2 degree in the region that is < 20 degree off the optical axis. In general, the attitude error of an onboard inertial system is less than 0.05 degree. In this case, the motion provided by the onboard sensor is adequate for slope estimation, and the motion refinement can be avoided (see Fig. 11).
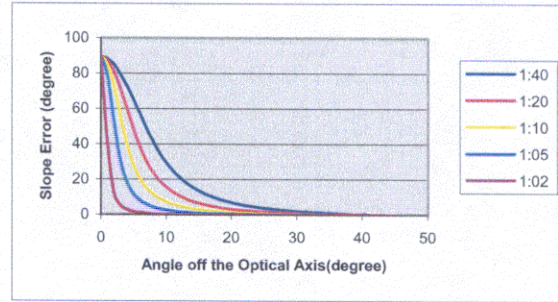

Figure 10: The relationship between the baseline to height ratio and the error of the slope estimation is shown here. In this case, the attitude error is 0.1 degree and the spacecraft is vertically descending.
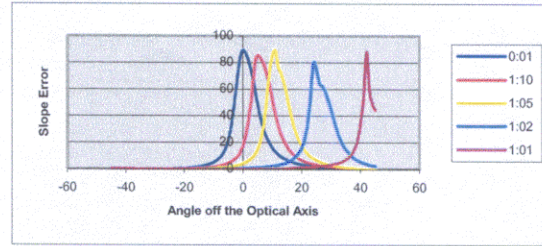

Figure 11: The relationship between the descent angle and the error of slope estimation. In this case, the attitude error is 0.1 degree and the baseline to height ratio is 1:20.

3 Experiments

3.1 Example 1

Three images were collected using the JPL vision group's Gantry test bed. The image size is 1024 by 1024 and the camera FOV is 33 degree. The first image was taken at about 100 cm above the ground, the second image was taken 10 cm left of the first image and the third image was down another 10 cm to simulate a 45 degree descent (see Fig. 12). We used the first and second image as a stereo pair to generate a range map of the surface (see Fig. 12) and this range data was used as a validation benchmark.
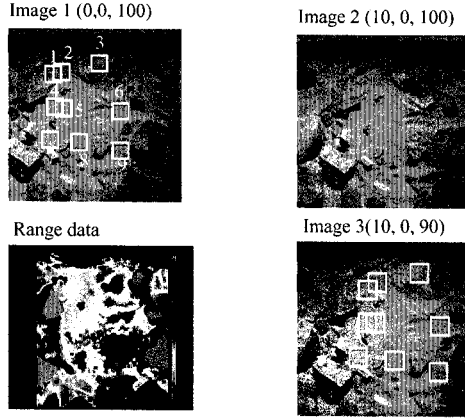
Image 1 (0,0, 100)   Image 2 (10, 0, 100)

Range data   Image 3(10, 0, 90)

Figure 12: A set of images was collected using the JPL vision group's gantry test bed Range data of the area is recovered by conventional stereovision, which is used as a benchmark.

The first and the third image were used as a descent image pair. Nine landing site candidates were selected from the first image using ISD and they were projected to the second image according to the motion and height. Then the nine homography transforms and associated slopes (S) were determined (see Table 1). In order to validate the result, the average slope (s) of the nine windows are also computed from the range data. In seven of nine windows, the differences between S and s are less than 3 degrees. The other two windows have slightly large difference (< 6 degrees) and the cause of it will be investigated later. Among the nine candidates, a favorable landing site can be selected.

Id	Col	Row	T	S	E	C	s
1	274	278	239	2.0	6.5	0.99	3.3
2	321	256	136	10.6	6.5	0.98	5.2
3	550	204	148	14.2	11.0	0.97	12.9
4	274	470	143	0.2	7.9	0.97	4.0
5	319	471	92	2.2	3.9	0.99	4.5
6	677	496	138	12.0	8.1	0.98	6.4
7	233	661	169	9.8	6.2	0.98	10.6
8	418	668	108	5.5	6.5	0.98	6.6
9	664	732	150	9.7	6.3	0.98	10.0

Table 1: The result of example 1, where Col and Row is the pixel coordinate of the candidate center in the first image, T is the texture index (ISD), S is the computed slope, E is the residual, C is the correlation between the two images, and s is the average slope computed from the range data.

3.2 Example 2

Another descent image pair collected near Silver Lake, California by a descending helicopter was used for experimental study (see Fig. 14). The image was taken about 220 meters above the ground and the lander size

was set to 10 meters. The results are listed in Table 2. It is interesting to point out that it failed to obtain a homography transform for window 5 because the helicopter shadow happened to be inside the window in the second image, which destroyed the correlation between the two windows. In order to prevent this problem from happening, the spacecraft's trajectory design should avoid following the sun ray direction so that its shadow would not be inside the landing area.
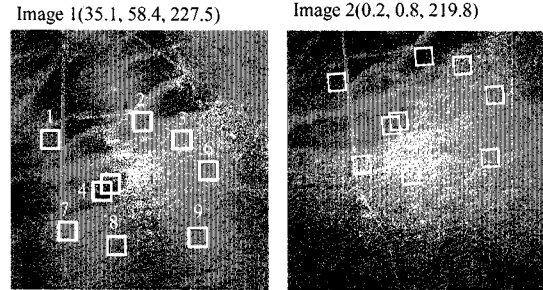

Image 1(35.1, 58.4, 227.5)   Image 2(0.2, 0.8, 219.8)

Figure 13: Two descent images collected near Silver Lake, California. The images were collected about 220 meters above the ground.

Id	Col	row	T	S	E	C
1	143	380	27	6.7	4.6	0.94
2	458	319	58	3.0	2.6	0.98
3	591	369	46	3.2	3.6	0.96
4	316	560	17	5.5	4.4	0.86
5	345	549	53	X	179.1	0.24
6	691	488	56	4.2	4.4	0.96
7	196	699	59	3.5	4.9	0.97
8	368	753	50	3.6	4.1	0.96
9	648	716	36	3.7	2.6	0.96

Table 2: The result of example 2.

3.3 The Speed Issue

To compute a total of 9 homography transforms takes about 1200 ms on a SUN Ultra 10 workstation. This speed is comparable with other methods, such as the lidar sensing method, and is adequate for safe landing purposes. However, when a slower computer is used, many strategies exist for reducing the computation. For example, some of the preprocessing, such as the image intensity gradient computation, can be moved to before the second image is taken. This is the reason why M_0 is faster to compute than M_1 in section 2.2. Another possible way to speedup the processing is to stop the computation of the homography transform once a suitable site is found. Additional strategies to speedup the processing will be investigated in the future.

4 Conclusions

In this paper, we presented a novel passive sensing approach for safe landing. The disadvantage of conventional passive imaging method has been successfully overcome. The experimental study shows this approach can accomplish the safe landing task in a comparable speed and reliability. Here we summarize the advantages and disadvantages of both active and passive sensing method in table 3.

Additional work is needed in this subject. For example, if the spacecraft is descending vertically, the slope estimation is very sensitive to the attitude error. In this case, motion estimation is needed, which could increase the computational burden substantially, so a new and fast algorithm would need to be developed here.

Furthermore, the robustness of this approach has not been adequately studied and its performance under different lighting conditions and different terrain types is needed to be studied. The final phase of this research will test the approach using a real Mars landing scenario.

Acknowledgements

Category	Active Sensing	Passive Sensing
Mass, Power Consumption, and Cost	High	Low
Data Resolution	Low	High
Data Processing Complexity	Low	Low to Moderate
Data Calibration Requirement	Yes (on line)	Yes (off line)
Illumination Constraints	No	Yes
Possible Blind Data Spot	No	Yes
Hardware Technology Readiness Level	Low	High

Table 3: A comparison between the active sensing and passive sensing.

References

[1] Clark Olson, L. Matthies, Y. Xiong, R. Li, F. Ma and F. Xu, "Multi-resolution Mapping Using Surface, descent, and Orbital Images", I-SAIRAS,2001.

[2] Richard Szeliski, "Video Mosaics for Virtual Environments", IEEE Computer Graphics and Applications, March 1996.

[3] Mars '05 Project Study Team, "Mars '05 Lander Mission/System Overview", March 2000.

[4] Mei Han and Takeo Kanade, " Homography-Based 3D Scene Analysis of Video Sequence", Proceeding of IEEE CVPR, 1998.

[5] Andrew Johnson, A. Klumpp, J. Collier and A. Wolf, "Lidar-based Hazard Avoidance for Safe Landing on Mars", AAS/AIAA Space Flight Mechanics Meeting, Feb 2001.

[6] Timothy Halbrook, J. Chapel, and J. Witte, "Derivation of Hazard Sensing and Avoidance Maneuver Requirements for Planetary Landers", AAS 09-024.

[7] Yves Dufournaud, C. Schmid, and R. Horaud, "Matching Images with Different Resolutions", IEEE CVPR, 2000.